

Accuracy of buffered-force QM/MM simulations of silica

Anke Peguiron,¹ Lucio Colombi Ciacchi,^{2,3} Alessandro De Vita,^{4,5} James R. Kermode,^{4,6} and Gianpiero Moras¹

¹Fraunhofer IWM, Wöhlerstraße 11, 79108 Freiburg, Germany

²Hybrid Materials Interfaces Group, Faculty of Production Engineering and Bremen Center for Computational Materials Science, University of Bremen, Am Fallturm 1, 28359 Bremen, Germany

³Center for Environmental Research and Sustainable Technology (UFT), 28359 Bremen, Germany

⁴Department of Physics, King's College London, Strand, London WC2R 2LS, United Kingdom

⁵CENMAT-UTS, Via Alfonso Valerio 2, 34127 Trieste, Italy

⁶Warwick Centre for Predictive Modelling, School of Engineering, University of Warwick, Coventry CV4 7AL, United Kingdom

(Received 27 November 2014; accepted 27 January 2015; published online 12 February 2015)

We report comparisons between energy-based quantum mechanics/molecular mechanics (QM/MM) and buffered force-based QM/MM simulations in silica. Local quantities—such as density of states, charges, forces, and geometries—calculated with both QM/MM approaches are compared to the results of full QM simulations. We find the length scale over which forces computed using a finite QM region converge to reference values obtained in full quantum-mechanical calculations is ~ 10 Å rather than the ~ 5 Å previously reported for covalent materials such as silicon. Electrostatic embedding of the QM region in the surrounding classical point charges gives only a minor contribution to the force convergence. While the energy-based approach provides accurate results in geometry optimizations of point defects, we find that the removal of large force errors at the QM/MM boundary provided by the buffered force-based scheme is necessary for accurate constrained geometry optimizations where Si–O bonds are elongated and for finite-temperature molecular dynamics simulations of crack propagation. Moreover, the buffered approach allows for more flexibility, since special-purpose QM/MM coupling terms that link QM and MM atoms are not required and the region that is treated at the QM level can be adaptively redefined during the course of a dynamical simulation. © 2015 AIP Publishing LLC. [<http://dx.doi.org/10.1063/1.4907786>]

I. INTRODUCTION

Chemically accurate descriptions of atomic-scale processes that can be used to inform the design of improved materials or processes are of ever-increasing demand. First principles methods such as density functional theory (DFT) have made huge contributions to our understanding of many of these processes.¹ However, today's supercomputers are restricted to modeling systems containing typically at most hundreds of atoms with currently available DFT tools, at least for dynamical simulations. Progress to date has mostly been made by focusing on materials properties which converge quickly with respect to system size. This is not always possible, as there are many problems where there is a tight, two-way “chemomechanical” coupling of local chemistry and long-range interaction, either elastic or electrostatic.^{2,3} The long-range nature of these forces means that the behavior of a small region, where a chemical process (e.g., breaking of a bond) takes place, can be influenced by the concerted behavior of very many atoms far away (e.g., the stress field driving a crack). Moreover, the reverse is also often true, with changes in the small region having direct consequences for the—potentially very many—atoms in the large region.

Materials failure problems are a prominent example of elastically coupled multiscale systems. Here, the coupling is indirect, and far exceeds the range of the individual

interactions between pairs of atoms. The need to represent the large stress gradients associated with, for example, grains in nanostructured metals,⁴ dislocation cores,⁵ or crack tips⁶ and their tight dynamical coupling with local chemistry necessitates the description of bond breaking reactions in systems containing 10^5 – 10^7 atoms. Electrostatic coupling, where long-range Coulomb interactions are insufficiently screened to be neglected, is common in biochemical systems^{3,7} but can also be important for polar solid-state materials such as silica and other oxides.⁸

The combined requirement of accuracy and efficiency can sometimes be met using classical reactive interatomic potentials (see, e.g., Refs. 9–11). However, in general, their transferability in chemically complex material systems is limited. In these cases, a quantum-mechanical description must be retained, at least in a localized region of the system, and hybrid quantum mechanics/molecular mechanics (QM/MM) schemes⁷ offer a solution. Most QM/MM approaches can be classified according to whether they combine QM and MM Hamiltonians by mixing energies or forces (schematically illustrated in Fig. 1). On the one hand, energy-mixing approaches, whether based on an additive, subtractive, or local-energy-mixing approach naturally conserve energy, provided that forces are correctly computed. Conversely, force-mixing approaches that combine MM forces in the MM region with QM forces in the QM region may conserve neither energy

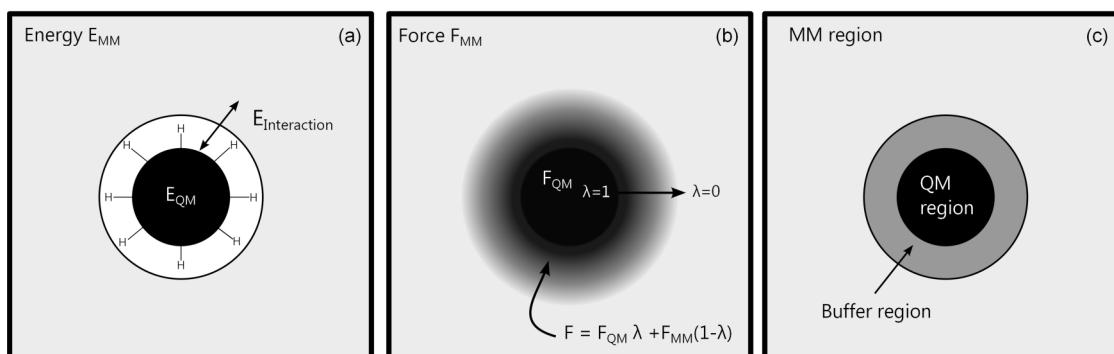


FIG. 1. Schematic representations of (a) energy-mixing and (b) force-mixing QM/MM approaches, with QM regions shown in black and MM regions in light gray. In the buffered force mixing approach (c), the QM region (black) is augmented by a buffer region (dark gray) which is then passivated to form the cluster used for QM force calculations. MM and QM forces are then assembled to give momentum-conserving forces for all atoms.

nor momentum. The conservation of momentum can be easily addressed by adjusting the forces so that they sum to zero (as explained in Sec. II).² On the other hand, force-mixing approaches are better suited to tackle two main issues in QM/MM simulations: (i) the “seamless coupling” of the two models and (ii) the “adaptivity” of the QM region. The latter denotes the possibility for atoms to enter and exit the QM region during a dynamical simulation. This is a desirable feature of a QM/MM scheme, as the QM region can in turn move and thus follow the motion of, for instance, a defect in a crystal.

Obtaining seamless coupling of QM and MM models requires a good mechanical matching between the models (e.g., ensuring the lattice and elastic constants are precisely aligned), as well as the elimination of the edge effects due to the artificial QM/MM boundary introduced by partitioning the system.¹² The latter depends on the details of the scheme. Force-mixing approaches have the distinct advantage that, provided that the MM and QM forces are correct, there are in principle no edge effects. Correct QM forces can be obtained by introducing a “buffer” region (Fig. 1(c)) which is added to the QM core region and then chemically passivated (for instance with H atoms for covalent solids) before carrying out each QM calculation.^{13,14} The size of the buffer should be chosen so that the forces in the core region are identical to those that would be obtained in a full QM calculation of the entire system. However, in practice, this can lead to unaffordably large QM clusters. The forces obtained in the QM calculation for the buffer region are then discarded and replaced with the MM forces on the same atoms. Provided that the QM core region has been adequately chosen (i.e., all parts of the system for which the MM model is inadequate are included in the QM core region), the MM forces can be expected to be more reliable than the QM ones in the buffer region, as they are not affected by the proximity of the QM/MM boundary. Conversely, for energy-mixing approaches, it is difficult to entirely eliminate edge effects. Here, the QM/MM interaction energy must typically be carefully tuned to lessen the effect of any broken covalent bonds crossing the QM/MM boundary, which relies on a delicate cancellation of errors to work correctly.¹³ As a result, achieving adaptivity of the QM region in conventional QM/MM methods is a challenging task. Recently, force-based schemes¹⁵ as well as energy-based methods that rely on the partitioning of a transition region between QM core and

MM regions, and on bookkeeping potential terms for energy conservation,^{15,16} have been used for this purpose in aqueous solutions. The buffered-force QM/MM method allows a moving QM region to be followed, providing a straightforward solution to the adaptivity problem in both solid systems² and aqueous solutions.¹⁷ Finally, if there is significant electrostatic interaction between QM and MM regions, the QM calculation should be performed in the electrostatic environment provided by the MM region. Typically this is done by adding classical point charges as an external potential in the self-consistent electronic minimization of each QM calculation.^{8,18,19} Care must be taken to avoid electron spill out.²⁰

Buffered QM/MM approaches have been applied to many materials problems, mostly so far where the coupling is elastic rather than electrostatic,² as in the case of crack propagation in silicon crystals.^{6,13,21–24} The same approach has been used to simulate water, where electrostatic embedding is crucial, but no covalent bond needs to be broken when partitioning the system in a QM and a MM region.¹⁷ To the best of our knowledge, only energy-based QM/MM approaches^{25,26} have been applied to polar materials such as silica, where both cut covalent bonds at the QM/MM boundary and electrostatic embedding need to be dealt with. In the latter case, attention has mostly focused on electronic properties or equilibrium geometry of defects rather than on mechanical properties. An accurate description of equilibrium geometric properties is typically easier to obtain than ensemble observables such as free energy differences, which are themselves a function of the forces used to propagate a dynamical simulation.²

Since buffered-force QM/MM (bf-QM/MM hereafter) has been shown to provide an improved description of free energy observables in comparison to conventional energy-based QM/MM (conv-QM/MM) in non-polar materials² as well as in polar liquids,¹⁷ we want to assess the accuracy of the bf-QM/MM approach in silica, an ubiquitous material in technological application and a prototypical example of a polar solid. A successful application of bf-QM/MM to silica would enable QM/MM dynamical simulations with an adaptive QM region. These could provide an improved understanding of materials failure processes in silica and of other processes where the description of silica in contact with liquids is relevant. Examples are stress-corrosion cracking²⁷ and the adsorption of molecules on silica surfaces, when both the full molecular structure

and local chemical reactions such as proton transfers need to be modeled simultaneously.²⁸

In this paper, we compare the accuracy of conv-QM/MM and bf-QM/MM on a number of silica model systems. The goal of hybrid simulations is to produce the same observables as if the entire system were modeled at the QM level. As a consequence, full QM results are used to validate the QM/MM results and the size of the test systems is limited by the maximum number of atoms that can be treated at the reference QM level. The rest of the paper is organized in the following way. The simulation methods are described in Sec. II. Next, we present a series of tests for the convergence of the bf-QM/MM forces to the full QM forces as a function of the buffer size for different silica systems (Sec. III). In Sec. IV, existing results for conv-QM/MM geometry optimizations of an oxygen vacancy in quartz are compared to bf-QM/MM results. Similar tests are presented for constrained geometry optimizations, where Si–O bonds in bulk quartz and on an amorphous silica surface are quasi-statically elongated (Sec. V). These simulations can be used to calculate potential energy barriers, and if they were extended to finite temperature, free energy barriers. Finally, in Sec. VI, the accuracy of conv-QM/MM and bf-QM/MM in molecular dynamics (MD) simulations of crack propagation in quartz is compared.

II. SIMULATION METHODS

A. QM and MM methods

Reference conv-QM/MM simulations are performed using the approach described by Zipoli *et al.*⁸ The QUICKSTEP scheme,²⁹ as implemented in the CP2K package,³⁰ is used to perform embedded and full QM calculations at the DFT level. The QUICKSTEP approach uses Gaussian-type orbitals for the expansion of the Kohn-Sham orbitals and a plane-wave representation of the charge density. We use the PBE approximation to the exchange-correlation potential,³¹ a plane-wave cutoff of 280 Ry, PBE-optimized GTH pseudopotentials,³² and the corresponding double-zeta valence polarization (DZVP) basis set.³³ A vacuum of at least 12 Å between QM atoms and their periodic images is used throughout, and electrostatic interactions between periodic images of the QM

cluster are decoupled and recoupled with the periodic images of the full MM system.¹⁹ For the MM Hamiltonian, we use the potential of van Beest, Kramer, and van Santen (BKS).³⁴ The extension of the BKS potential from Hassanali *et al.*,³⁵ which was devised for amorphous silica surfaces in contact with water, is used to describe amorphous silica with hydroxylated surfaces. Here, in the absence of water, the three-body Si–O–H term is replaced by an harmonic angle term. All bf-QM/MM simulations are performed using the QUIP code³⁶ as a “driver” for the CP2K package, although this functionality has been very recently implemented directly in the CP2K and AMBER codes.³⁷ Geometry optimization simulations are performed with the Fast Inertial Relaxation Engine (FIRE),³⁸ which only requires forces for the minimization procedure.

B. QM/MM coupling

We consider two alternative ways to chemically saturate the dangling bonds that are artificially created when the QM region is carved out of the system. The simplest approach is to build neutral clusters by selection of QM regions consisting of complete SiO₄ tetrahedra. These are chemically passivated by replacing [–Si–O]–Si bonds crossing the QM/MM boundary with [–Si–O]–H (where square brackets denote the atoms inside the QM region). We refer here to this approach as cluster embedding (CE) (Fig. 2(a)). When additional classical electrostatic forces between QM and MM atoms are added to the QM forces, the approach is also referred to as mechanical embedding.³⁹

However, potentially long-range electrostatic forces in polar materials can influence the electronic structure in the QM region. As a consequence, it can be useful to include the electrostatic field of the MM region directly in the QM calculation. If the CE strategy outlined above were followed, the H passivation atoms would be located very close to the embedding charges arising from the Si atoms just outside the QM region, which could cause electron spill out. Zipoli *et al.*⁸ suggested an alternative termination strategy that addresses this issues by replacing the boundary O atoms with a special O* boundary species with an extra electron to saturate the valence, and a corresponding increase in ionic charge to retain overall (QM + MM) charge neutrality. The combination of this

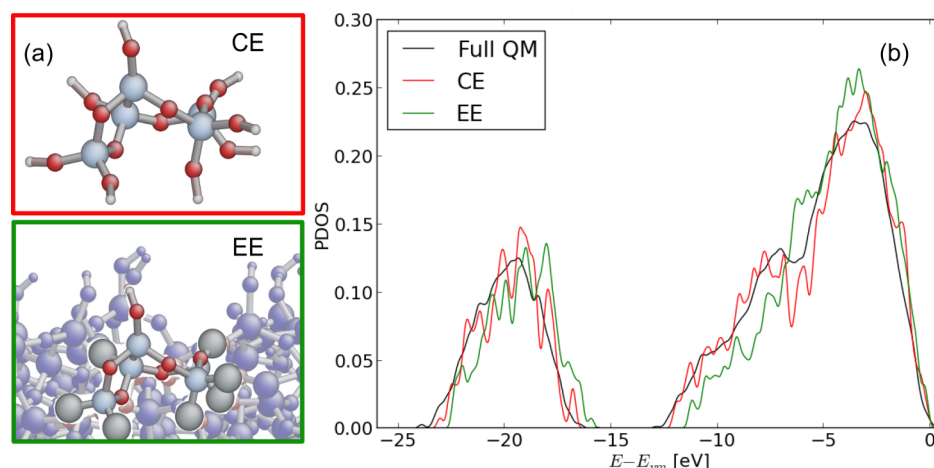


FIG. 2. (a) Illustration of different QM/MM embedding schemes: CE and EE, where the O* are represented by gray spheres. See text for full details of the two schemes. (b) The PDOS on a Si atom in a bulk quartz-sample at 1000 K is calculated with CE and EE for a QM region of 7 Å and compared to the full QM result. Here, E_{vm} is the valence-band maximum.

passivation scheme and the external electrostatic environment provided by the MM point charges is denoted by electrostatic embedding (EE).

We first test the CE and EE approaches by comparing the projected density of states (PDOS) obtained with both embedding strategies with those of a reference full QM calculation for a quartz sample thermalized at 1000 K. The PDOS on a Si atom located at the center of a spherical QM region (with a 7 Å radius) is plotted in Fig. 2. The general structure of the QM PDOS is qualitatively reproduced by both the CE and EE QM/MM calculations, although the simple CE reproduces more accurately the PDOS structure between -10 eV and -5 eV.

We next move to an amorphous silica surface system, where we use the Mulliken population analysis to check how the charge density at the center and near the boundary of the QM region is reproduced by a QM/MM calculation compared to a reference QM calculation. For conv-QM/MM with the EE approach, MM charges are used as embedding charges for the QM calculation. This ensures overall charge neutrality of the combined QM/MM system. Depending on which silica potential is used, the MM charges span a wide range (e.g., oxygen charges are -0.45 e and -1.2 e for the CHARMM water contact angle (CWA) ⁴⁰ and BKS ³⁴ force fields, respectively). We note that, since these different charges may be well suited to reproduce particular properties they have been fit to (i.e., the water contact angle on a silica surface or the structural bulk properties of quartz in the above examples), the choice of the MM potential introduces some arbitrariness in the choice of embedding charges used for a conv-QM/MM calculation. In the bf-QM/MM case, we focus on the calculation of accurate QM and MM forces rather than on the definition of a total QM/MM energy. As a consequence, the QM and MM calculations can be carried out independently and it is not necessary to use the MM charges as embedding charges in the EE of the QM region. In fact, the embedding charges can in principle be tuned in order to improve the accuracy of the QM force calculation, provided that the charge neutrality in the latter is ensured. To test this, we compare EE results using two choices of embedding charges: (i) the average QM Mulliken charges in the MM region, as determined from the reference QM calculation on the full systems; (ii) the charges of the BKS MM potential. Here, we note that there is only one free parameter, since $q_O = -1/2q_{Si}$ and $q_H = 1/4q_{Si}$ must be enforced to ensure charge neutrality of both bulk SiO_2 and OH-terminated SiO_2 slabs or clusters. The average Mulliken q_{Si} in the full QM calculations varies from 1.10 e to 1.28 e depending on the silica system (bulk or surface), and is in good agreement with previously published results.⁴¹

We find that the embedding scheme has little influence on atoms located at the center of the QM region, where the maximum deviation from the QM reference charge value is for all three schemes below 0.002 e for the bulk and 0.02 e for the amorphous surface. The average Mulliken charge errors are summarized in Table I for oxygen atoms located at the boundary of the QM region. Here, the EE with Mulliken embedding charges performs best in reproducing the Mulliken charge in both bulk quartz and the amorphous silica surface. This embedding approach will be used throughout this paper,

TABLE I. Average Mulliken charge error (in units of electron charge) with respect to full QM results for different embedding strategies on oxygen atoms located at the boundary of the QM region.

	CE	EE	EE
		BKS charges	Mulliken charges
Bulk quartz (170 QM atoms)	0.089 ± 0.011	0.129 ± 0.009	0.057 ± 0.004
a- SiO_2 surface (100 QM atoms)	0.072 ± 0.023	0.138 ± 0.033	0.044 ± 0.026

particularly because long-range electrostatic interactions are likely to be especially important to correctly describe the interaction between silica surfaces and polar liquids envisaged as a future application of this work.²⁸

As mentioned in Sec. I, an important difference between energy-based and force-mixing QM/MM approaches is that, while the former methods are normally energy conserving, force-mixing approaches may conserve neither energy nor momentum. In bf-QM/MM MD simulations, we use a simple way to enforce momentum conservation. The sum of all atomic forces, which is generally nonzero, is divided by the number of atoms. This small quantity is then subtracted to each atomic force, thus restoring momentum conservation.

C. Silica model systems

In Secs. III–VI, the accuracy of conv-QM/MM and bf-QM/MM is compared on a number of silica model systems. In Sec. III, we assess the accuracy of bf-QM/MM forces on three silica systems: (a) a bulk quartz sample, where atomic positions were previously randomly perturbed; (b) an hydroxylated amorphous silica slab; (c) an hydroxylated amorphous silica slab in contact with water. We choose system sizes of about 10^3 atoms in order to be able to perform the full QM reference force evaluation. The bulk quartz sample consists of a cubic quartz cell containing about 2600 atoms, where we initially slightly randomized the atomic positions and then thermalized the system in the NVT ensemble for about 100 fs at a temperature of 1000 K. To do this, we used a short-ranged version of the polarizable potential for silica first developed by Tangney and Scandolo.^{10,42} The amorphous slab contains about 1400 atoms and was obtained following the procedure described in Ref. 43. To produce the silica/water interface, the vacuum of about 22 Å between the slab's top and bottom surfaces was filled with 840 randomly positioned water molecules. While keeping the silica surface fixed, the water was thermalized for 400 fs at 400 K.

The quartz system used for the oxygen vacancy (Sec. IV) and bond elongation (Sec. V) simulations is a 1350-atom $5 \times 3 \times 5$ supercell of the 18-atom α -quartz orthorhombic cell. The optimal QM lattice constants ($a = 4.872$ Å and $c/a = 1.102$) were determined with a cell optimization on the $3 \times 3 \times 3$ supercell of the 9-atom α -quartz trigonal unit cell. For the crack propagation simulations described in Sec. VI, we use a 768-atom α -quartz crack slab with dimensions $54 \times 32 \times 4.84$ Å³, periodic along the crack front and the crack propagation direction. The slab contains a penny-shaped nanoscale seed crack opening on the (0001) basal cleavage plane and

an initial uniaxial strain of 26.8% is applied in the vertical direction.

III. ACCURACY OF BF-QM/MM FORCES

To assess quantitatively the effectiveness of the bf-QM/MM approach, the accuracy of the atomic forces in the QM region has to be tested as a function of the size of the buffer (i.e., the distance between the edge of the QM core region and the artificial QM/MM boundary). In other words, we want to know if and how rapidly the forces calculated with the bf-QM/MM method converge to the atomic forces obtained by means of a full QM calculation. To reach a compromise between accuracy and computational cost of the simulation, the practical target is to operate with a buffer radius that allows the difference between bf-QM/MM forces and full QM reference forces to be lower than 0.1 eV/\AA , as this is the typical accuracy of DFT forces for the material systems under investigation. Previous accuracy tests were performed on a number of Si and Si/H systems,^{44,45} as well as on water.¹⁷ As shown in Fig. 3 for Si and in Ref. 17 for water, a buffer region size of 5–7 \AA is sufficient to reach the 0.1 eV/\AA force-accuracy target for these systems.

We perform similar force-accuracy tests on different silicon oxide model systems. Namely, we consider the systems described in Sec. II: (a) a bulk quartz sample, where atomic positions were previously randomly perturbed (Fig. 4(a)); (b) a hydroxylated amorphous silica slab (Fig. 4(b)); (c) a hydroxylated amorphous silica slab in contact with water (Fig. 4(c)). The average magnitude of the DFT atomic forces on the three test systems is of the order of 1 eV/\AA . As for the Si and Si/H cases mentioned above, we select a set of atoms for each of the test systems and calculate the forces for each of these atoms by growing spherical QM regions of increasing size around them. In this case, the QM core consists of a single atom and therefore the buffer size and the radius of the QM region coincide. This is equivalent to testing the accuracy of the forces on atoms located at the boundary of a QM core region of any size.⁴⁴ The atomic forces evaluated in this way for various buffer sizes and

the two different embedding schemes described earlier are then compared to the forces calculated on the same atoms by means of a full QM calculation.

In Fig. 4, the force errors (i.e., the difference between the bf-QM/MM forces and the target QM ones) for the single test atoms and the average force error are plotted as a function of the buffer region size for the three test systems. The test atoms are silicon atoms (i.e., centers of silica tetrahedra) for the quartz case (Fig. 4(a)), and oxygen atoms belonging to surface silanol groups for the amorphous silica slabs (Figs. 4(b) and 4(c)). In the case of the silica slab in contact with water, only complete water molecules are included in the QM regions (i.e., no water covalent bond is cut). In general, we note that the mean force error decreases with increasing buffer sizes. As in the aforementioned Si and H_2O cases, significant force errors are found for small buffer radii ($\sim 2 \text{ \AA}$). The different magnitude of the force errors in the three systems correspond to different values of the average force magnitude on test atoms for the three systems (labelled on the graphs in Figs. 4(a)–4(c)), with smaller errors obtained for smaller values of the average force. Average force errors smaller than 0.2 eV/\AA can only be obtained for buffer sizes of about 8 \AA , while buffer sizes of 12 \AA are needed to achieve force errors lower than 0.1 eV/\AA . This shows that larger buffer radii than in the Si and H_2O cases are needed to achieve reasonably accurate force evaluations, resulting in a larger computational cost. However, the bf-QM/MM approach helps to systematically improve the accuracy of QM/MM force calculations and the use of a buffer region is apparently more crucial than the details of the embedding scheme used. As shown in Fig. 4, EE plays a minor role in the accuracy of the QM/MM calculations. While EE yields smaller force errors for all values of the buffer radius in the bulk quartz case, for which the method has been designed and tested so far,^{8,26} it only becomes slightly more accurate than CE for large radius values in the silica slab cases. This might be due to the EE only taking into account fixed point charges; further tests including higher order multipoles or variable charges would be of interest (e.g., including electrostatic response up to dipole order has been shown to significantly improve the accuracy of force fields for silica⁴²).

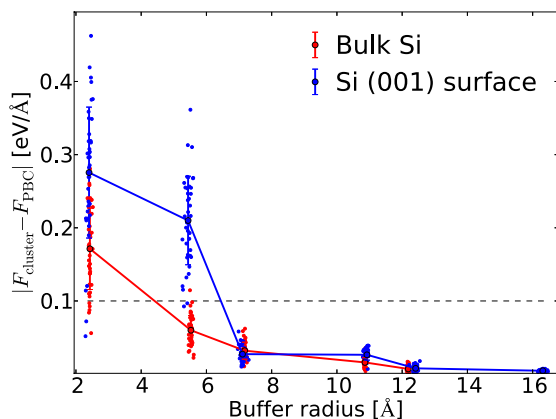


FIG. 3. Difference between forces calculated using a finite cluster and forces calculated with a full periodic QM calculation as a function of the buffer radius. The test systems are bulk silicon and its (001) surface. Only CE is used here and clusters are chemically terminated with H atoms. Small dots represent force errors on different Si atoms, while solid lines show the average error. The dashed horizontal line shows the target accuracy of 0.1 eV/\AA .

IV. QM/MM GEOMETRY OPTIMIZATION OF A NEUTRAL OXYGEN VACANCY IN QUARTZ

As a first test simulation of a silica system, we calculate the relaxed geometry of a neutral oxygen vacancy in bulk α -quartz with bf-QM/MM and conv-QM/MM (details about the model system are provided in Sec. II and Figs. 5(a) and 5(b)). We then compare the results of the QM/MM simulations with the full QM geometry. This example is of particular interest because: (i) the reference conv-QM/MM technique⁸ provides accurate results on this model system despite the generally large force errors in the vicinity of the QM/MM boundary (see Fig. 4) and (ii) the QM and MM models are not elastically matched (i.e., they yield different elastic constants). The main motivation of this test is to check whether bf-QM/MM can be used to improve the accuracy of the conv-QM/MM geometry optimization. For this reason, we do not make any attempt in

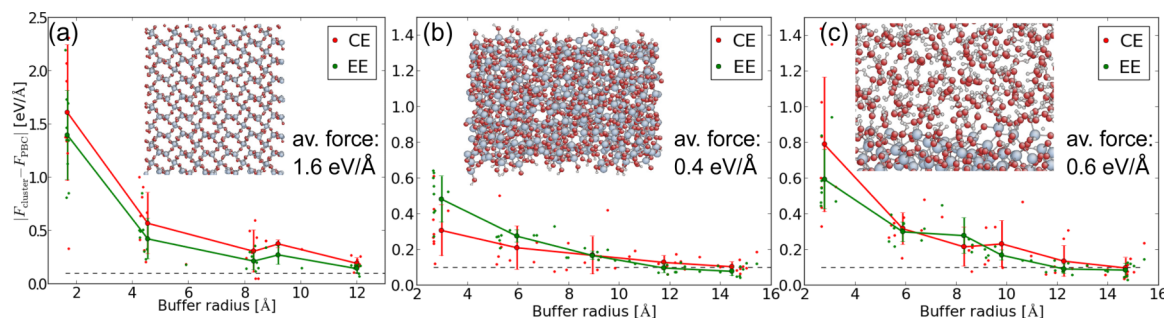


FIG. 4. Absolute error in a bf-QM/MM calculation with respect to a full QM force calculation as a function of the buffer size. The test systems are (a) thermalized α -quartz, (b) a hydroxylated amorphous silica slab, and (c) the same slab in contact with water. Red and green dots represent force errors on individual atoms for CE and EE, respectively. The solid lines show the average force error. The dashed black line indicates the target force error of 0.1 eV/Å.

this work to elastically match the QM and MM models. This leads to intrinsic errors in the atomic positions in the QM region but does not affect the goal of this test.

We relax the atomic positions for different sizes of the QM and of the buffer regions. In Table II, we report relative errors with respect to the full QM geometry in the Si–Si bond length at the vacancy site (Fig. 5(c)), as well as in the Si–O bond lengths and Si–O–Si angles in the QM region. We consider conv-QM/MM simulations with 12, 50, and 169 atoms QM regions centered on the vacancy site.⁴⁶ For the two smaller QM regions, we also perform bf-QM/MM simulations with buffer sizes of 3.6 and 5.7 Å.

In general, errors in the Si–Si and Si–O bond lengths are very small even for conv-QM/MM with the smallest QM region. The errors on the Si–O–Si angles are larger and probably due to the elastic mismatch between the QM and the MM models. Increasing the buffer size during the bf-QM/MM calculation systematically decreases the magnitude of the errors. For calculations with the same computational cost (e.g., conv-QM/MM with a 50-atom QM region and bf-QM/MM with 12-atom QM region and 3.6 Å buffer), no relevant difference is observed. The Si–O bond length distributions calculated in a 44-atom area centered on the vacancy (corresponding to the QM core region in the bf-QM/MM calculation) with the MM, QM, conv-QM/MM, and bf-QM/MM methods is shown in the histograms of Fig. 5(d). The different peaks of the MM and QM distributions show the effect of the elastic mismatch between the two models. While the conv-QM/MM

distributions are quite broad, the peaks obtained by bf-QM/MM are less broad and closer to the full QM result. However, in this case, the accuracy of the conv-QM/MM is satisfactory and the missing elastic matching between the QM and MM models seems to be more relevant than spurious effects at the QM/MM boundary. This might be due to the displacement field generated by the vacancy being short-ranged and therefore not affected by the boundary of the relatively small QM region.

We note that the conv-QM/MM scheme needs a special-purpose potential energy function that suitably describes the coupling between the QM and MM regions. The choice of this potential depends on the particular choice of the Hamiltonians and on the system under investigation. In the QM/MM formulation of Zipoli *et al.*,⁸ a short-ranged two-body potential with the BKS analytical form was specifically parametrized to describe the interaction between O* atoms in the QM region and their first Si neighbors in the MM region. This “linking” potential was used for all conv-QM/MM calculations described below, except where otherwise stated. If this two-body term is replaced by the original BKS two-body term, the QM and MM regions detach during geometry optimization. However, the addition of a stiff harmonic two-body term ($V = k(r - r_0)^2$ with $k = 34.7$ eV/Å² and $r_0 = 1.59$ Å) to the original BKS term between O* pseudoatoms and MM-Si atoms prevents the detachment of the QM and MM regions and yields geometries that are as accurate as those obtained with the O*–Si term devised in Ref. 8. Using the bf-QM/MM scheme does not imply any additional computational cost with respect to

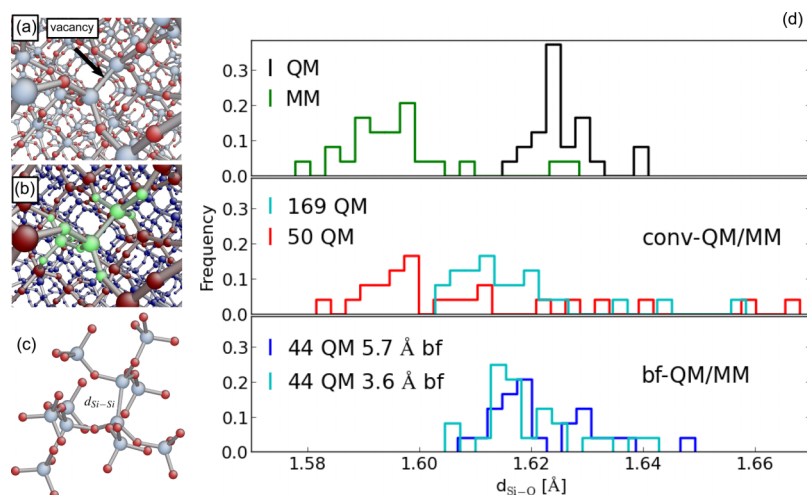


FIG. 5. Geometry optimization of the neutral vacancy in α -quartz (a) (Si atoms: gray; O atoms: red). The QM region in conv-QM/MM and bf-QM/MM simulations is centered on the Si–Si bond located at the vacancy (b) (QM atoms: green; buffer atoms: red; MM atoms: blue). The O*–terminated 50-atom cluster used for the conv-QM/MM calculation is shown in panel (c). The Si–O bond-length distributions in a 44-atom area centered on the vacancy for the QM, MM, conv-QM/MM, and bf-QM/MM schemes are reported in panel (d).

TABLE II. Si–Si bond length in the neutral vacancy in α -quartz and average errors on Si–O distances and Si–O–Si angles for different QM/MM schemes and computational costs. Values denoted by (\star) are obtained with a potential term for the QM/MM linking that consists of the sum of the original BKS potential and a harmonic potential (see text for details). Values denoted by (\dagger) are taken from Ref. 8.

Method	QM core (atoms)	QM radius (Å)	Cost (atoms)	$d_{\text{Si-Si}}$ (Å)	Errors w.r.t. QM (%)		
					$d_{\text{Si-O}}$	$d_{\text{Si-O}}$	$\alpha_{\text{Si-O-Si}}$
QM	1349		1349	2.39			
conv-QM/MM	12	4.7	12	2.36	1.4	1.1	7.5
	50	7.3	50	2.36	1.3	1.5	7.2
(\star)	50	7.3	50	2.37	1.0	1.6	6.2
	169	9.9	169	2.34	2.0	1.0	6.1
(\dagger)	9-54		9-54	2.35-2.40			
Buffer radius							
bf-QM/MM	12	3.6	50	2.34	2.2	0.8	7.4
	12	5.7	169	2.38	0.4	0.7	6.6
	44	3.6	169	2.37	1.1	0.4	5.4
	44	5.7	375	2.40	0.2	0.3	4.4

the conv-QM/MM scheme at the same level of accuracy and has the advantage of not requiring the parametrization of this coupling term.

V. QUASI-STATIC SIMULATIONS OF BOND ELONGATION

After the comparison of the two QM/MM approaches on systems with relaxed atomic positions, we perform a series of geometry optimization tests whereby the length of a Si–O bond located at the center of the QM region is constrained. Following the approach used by Bernstein *et al.* for Si,² we relax the atomic positions for increasing values of the

constrained Si–O bond length and measure the force on the constraint. This is an interesting test because, if the Si–O bond length is a representative reaction coordinate, the forces on the constraint can be integrated along the minimum energy path (MEP) and provide a potential energy barrier even when a total energy is not defined, as in the bf-QM/MM case. The approach can also be extended to calculate free energy barriers by performing ensemble averaging of the constraint forces during finite temperature MD simulations. In this way, we perform two series of tests on two model systems: bulk α -quartz and a hydroxylated amorphous SiO₂ surface. In the first series of tests, we use the conv-QM/MM scheme to measure the constraint force on the atomic positions obtained by means of a full-QM calculation. This test is similar to those presented

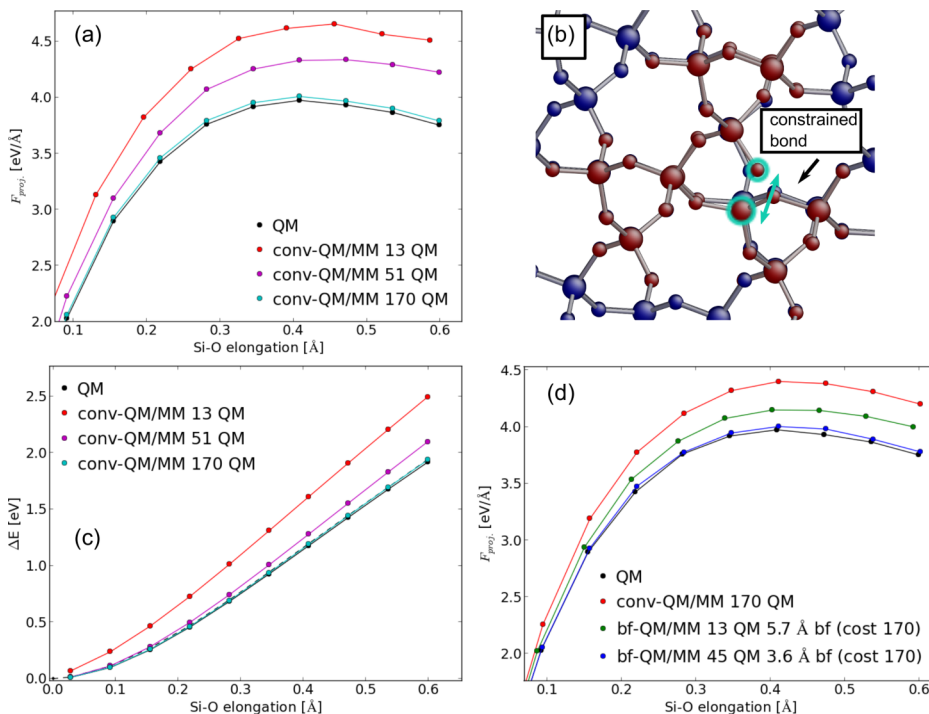


FIG. 6. (a) Constraint forces along a Si–O bond in bulk α -quartz (b) as a function of bond elongation. Here, conv-QM/MM force calculations are performed on the full-QM geometries. In panel (c), the integrated energies along the path are plotted. For the full QM calculation, as a reference, we also plot the potential energy calculated directly (dashed line). Constraint forces obtained from independent QM, conv-QM/MM, and bf-QM/MM are plotted in panel (d).

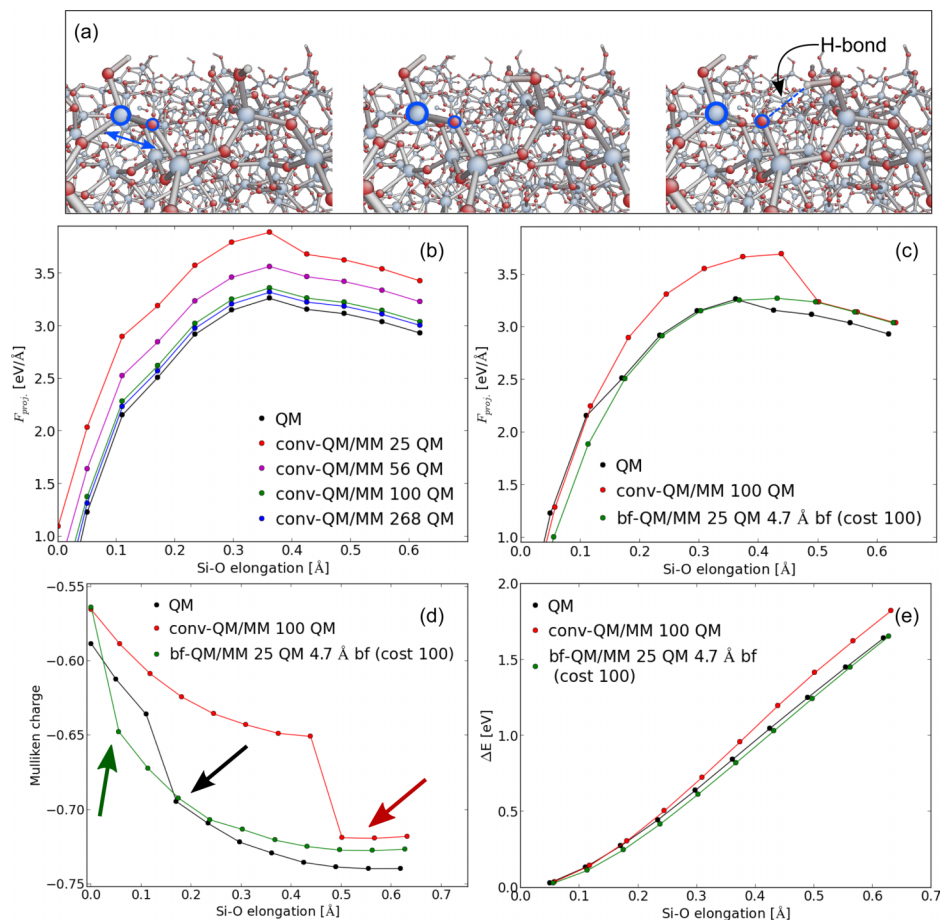


FIG. 7. (a) Snapshots from QM constrained geometry optimizations, where the blue atoms are constrained to a fixed distance. The dashed blue line in the left snapshot indicates a hydrogen bond. (b) Constraint forces calculated with QM and conv-QM/MM schemes on the QM trajectory. Panels (c)-(e) show constraint forces, Mulliken charges on the O atom and energies as a function of bond elongation for QM, conv-QM/MM, and bf-QM/MM calculations.

in Sec. III and provides information on how far the QM/MM boundary must be from the constrained bond in order not to affect the accuracy of the force calculation. Once a QM region size that ensures an accurate constraint force calculation is determined, we perform independent conv-QM/MM and bf-QM/MM constrained geometry optimization simulations with the same computational cost and compare the evolution of the force during bond elongation to the full-QM case.

The results for the α -quartz case are summarized in Fig. 6. The force acting on the constraint is plotted as a function of the bond elongation in Fig. 6(a). Here, the QM forces are compared to the conv-QM/MM forces calculated on the atomic positions obtained with the full QM calculations. Three different sizes of the QM region, which is approximately centered on the constrained bond (Fig. 6(b)), are considered. The error between conv-QM/MM and full QM forces decreases for increasing QM region sizes. A QM region composed of 170 atoms (i.e., a distance between constrained bond and the QM/MM boundary of about 10 Å) is necessary to correctly reproduce the QM forces (within an absolute average error of 0.04 eV/Å, cyan line). This is consistent with the buffer size suggested by the tests in Sec. III. Smaller QM regions, consisting of 13 and 51 atoms (with radii 4.7 Å and 7.3 Å respectively), are too small and yield average errors of 0.31 eV/Å and 0.80 eV/Å, respectively. Similar considerations apply to the results of the force integration along the reaction path plotted in Fig. 6(c). Here, the accuracy of the force integration procedure can be assessed by comparing the QM energies as obtained by

force integration (black line) with the direct QM total energies (black dashed line). The 170-atom QM region, which accurately reproduces the QM forces on the QM geometries, is then used to carry out independent conv-QM/MM and bf-QM/MM quasi-static bond-elongation simulations. For comparison, one conv-QM/MM and two bf-QM/MM simulations with the same computational cost (i.e., 170 QM atoms) are performed for two different sizes of the buffer region, and compared to the full QM results. The constraint force as a function of the Si-O elongation is plotted in Fig. 6(d) for the four different calculations. The conv-QM/MM forces (red line in Fig. 6(d)) are affected by an average error of 0.32 eV/Å. The average force error decreases for the bf-QM/MM: the error is 0.12 eV/Å, for a 13-atom QM region and a 5.7 Å buffer (green line in Fig. 6(d)) and 0.03 eV/Å, for a 45-atom QM region and a 3.6 Å buffer (blue line in Fig. 6(d)). This shows that, although a 170-QM-atom conv-QM/MM simulation is able to accurately reproduce the forces at the center of the QM region (Fig. 6(a)), using forces on QM atoms close to the QM/MM boundary to perform the geometry optimization can lead to considerable errors with respect to the full QM result: here equivalent to an error of about 0.2 eV in the integrated energy difference. More accurate results can be obtained at the same computational cost using the bf-QM/MM scheme, where the QM forces on atoms in the buffer region are replaced by the MM forces. However, the bf-QM/MM method can accurately reproduce the QM results only if the size of the QM core region is large enough (45 atoms here).

The same simulations are also performed on an amorphous silica slab with hydroxylated surfaces. In this case, the constraint is applied to a Si–O bond that involves an OH-terminated Si atom and an O atom of a surface siloxane group (Fig. 7(a)). As described in the quartz case above, we first perform a series of QM geometry optimization simulations for increasing lengths of the constrained bond. Upon elongation of the Si–O bond, a H atom of a nearby silanol group reorients towards the O atom to form a hydrogen bond (snapshots are shown in Fig. 7(a)). Also in this case, conv-QM/MM calculations with a QM region larger than 100 atoms are necessary to reproduce the force evolution on the QM positions, Fig. 7(b). This corresponds to a QM region radius of about 12 Å, which is once again consistent with the results described in Sec. III. It is important to note that the smallest QM region used here is large enough to include the silanol group involved in the H-bond formation. As in the quartz system, the constrained geometry optimization simulations are then repeated using the conv-QM/MM scheme with a 100-atom QM region and the bf-QM/MM scheme with a 25-atom QM region and a 4.7 Å buffer region (for a total computational cost of 100 QM atoms). The constraint forces, the Mulliken charges on the O atom of the constrained Si–O bond and the energy profiles obtained by force integration are plotted in Figs. 7(c)–7(e) as a function of the Si–O bond elongation. The aforementioned formation of a hydrogen bond is characterized by a sudden decrease of the constraint force and of the oxygen’s Mulliken charge. This happens at an elongation of about 0.15 Å for the QM case (black lines). The bf-QM/MM scheme is able to reproduce the constraint forces and the H-bond forms at about 0.05 Å elongation (green lines). For the conv-QM/MM method (red line), this happens at a larger elongation (0.5 Å), resulting in higher constraint forces up to that point.

VI. FINITE TEMPERATURE QM/MM MD SIMULATIONS OF CRACK PROPAGATION IN QUARTZ

We have shown in Sec. III that substantial force errors arise at finite temperatures when using energy-based QM/MM approaches in materials systems such as silica, and this is likely to have adverse consequences for the accuracy of dynamical simulations. Here, we consider a non-equilibrium case where the trajectory followed by a simulation is particularly sensitive to the accuracy of the forces used: brittle crack propagation. Accurate fracture simulations must describe bond-breaking reactions in systems containing of the order of 10^6 atoms, which can often only be accomplished using QM/MM approaches.

To investigate the suitability of the two QM/MM approaches considered here to describe bond-breaking processes at a crack tip, we select a much smaller model system, which allows direct comparison to a reference QM simulation (details are provided in Sec. II and in Fig. 8(a), left panel). While there is a strong case for using adaptive bf-QM/MM for these kinds of problems to allow a moving QM region which tracks the tip of a moving crack,⁶ here we fix the set of QM atoms to allow comparison with energy-based approaches where the QM region cannot be changed during the course of a simulation.

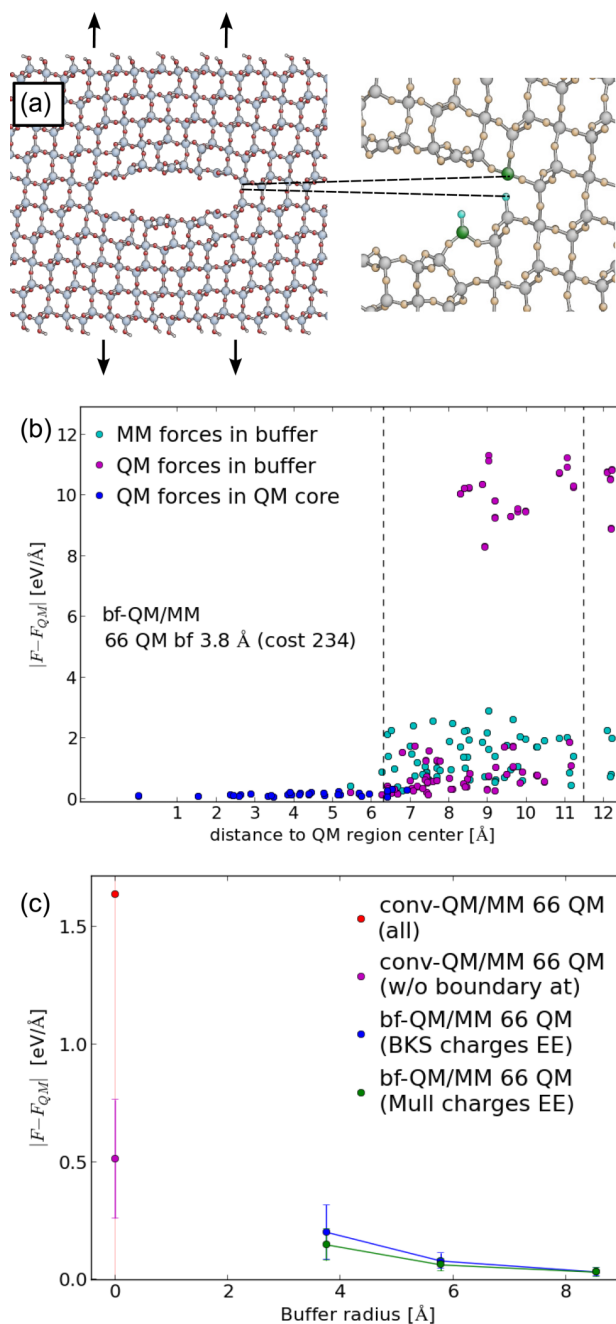


FIG. 8. (a) Bond breaking at the crack tip in a strained α -quartz slab. Left panel: initial relaxed QM geometry (red, gray, and white spheres represent O, Si, and H atoms, respectively). Right panel: snapshot of the crack tip just after bond breaking (brown and gray spheres are two-fold and four-fold coordinated atoms, respectively; green spheres are three-fold coordinated atoms, while blue spheres are atoms with one bond). (b) bf-QM/MM force errors with respect to the full QM forces for one representative system configuration. Here, different colors refer to QM forces in the QM-core region, QM forces in the buffer region, and classical forces in the buffer region. The vertical dashed lines show the average radius of the QM-core and buffer regions. In panel (c), the force errors as a function of buffer radius are averaged over several configurations. Here, conv-QM/MM errors with no short-range QM/MM boundary linking potential are shown as comparison. The error bar for the conv-QM/MM measured on the full QM region (including QM boundary atoms; red dot) extends up to 4.8 eV/Å and is not fully shown.

After an initial geometry relaxation, with an initial uniaxial strain of 26.8% in the vertical direction, we carry out finite-temperature MD simulations with random initial velocities sampled from a Maxwell-Boltzmann distribution at a

temperature of 300 K, first with the reference QM Hamiltonian and later with the conv-QM/MM and bf-QM/MM approaches. Atoms in the top and bottom rows of the slab are fixed, and an uniaxial strain increasing at a rate of 10^{-4} /fs is imposed during the 700-fs-long simulations. We note that the large initial strain, high strain rate, and small system size used here do not allow direct comparison with experimental fracture toughness measurements, but nevertheless permit comparisons between different modeling approaches. In contrast to the constrained minimizations reported above, the forces near the QM boundary are not zero during dynamics, so we expect that systematic errors there may lead to more severe consequences.

The system quickly equilibrates to half the initial temperature (Fig. 9(a), upper panel, green line) as expected by the equipartition theorem, and then remains relatively constant despite the heat produced by the work done by the moving boundaries (note that, to allow comparison of trajectories, no thermostats were applied in any of the simulations described here). Fig. 9(a) also shows the length of the Si–O bond immediately in front of the crack tip (lower panel, green line), which breaks when the strain reaches 33%, leading via a crack advance step to the configuration illustrated in Fig. 9(c).

We next look at the accuracy of the forces obtained with the bf-QM/MM approach for a configuration just before the first bond-breaking event in the reference QM trajectory. It is clear from Fig. 8, which shows the force errors as a function of the distance from the crack tip, that the method gives accurate forces (blue circles) for atoms more than about 6.5 \AA inside the QM/MM boundary (vertical dashed line). This corresponds to the average radius of the QM core region in the bf-QM/MM calculation. The error in the QM forces increases as one moves closer to the QM/MM boundary (magenta circles). We note that no additional QM/MM linking potential term is used in the bf-QM/MM calculation. This allows us to show that in a bf-QM/MM simulation if QM forces in the buffer (i.e., between the two vertical dashed lines) were not discarded, they would be affected by a very large error. This is why in bf-QM/MM simulations only QM forces on atoms that are sufficiently far away from the boundary (blue circles) are used. QM forces in the buffer region are replaced with the MM forces (cyan circles), which are in this case closer to the reference QM forces, providing of course that the size of the QM region is chosen appropriately.

The average force error on QM region atoms for conv-QM/MM (red dot, zero buffer, also in this case no additional

QM/MM linking potential term is used for comparison) and bf-QM/MM is plotted in Fig. 8(c), for configurations taken from 16 snapshots of the reference QM trajectory (starting at a strain of 32.23%). The bf-QM/MM force errors are plotted for both BKS (blue circles) and Mulliken charge EE (green circles). As before, we find that using the average Mulliken charges of a reference QM calculation for the EE leads to slightly more accurate forces. While the MM forces can be systematically improved (e.g., by using a different classical potential¹⁰), the large force errors near the boundary of the QM region are a general consequence of the truncated QM calculation. One can imagine finding the best possible short-range potential that properly links the QM and MM regions, as reported above for the conv-QM/MM geometry optimizations. In this spirit, we discard the boundary atoms from our force-error analysis and show the remaining average force-error (magenta circles). However, in general, unlike in the vacancy geometry optimization, it is extremely challenging to fit these linking functions once-and-for-all in such a way that they remain valid throughout a MD simulation and are able to reliably reproduce the non-zero QM forces on the QM boundary atoms. Instead, the buffer allows us to simply discard these generally inaccurate forces.

To demonstrate this, we re-ran the fracture dynamics with the trad- and bf-QM/MM methods exactly as described above. For the bf-QM/MM, we use a buffer size of 5.8 \AA (i.e., the buffer/MM boundary is about 12 \AA away from the crack tip). As in the geometry optimization simulations presented in Sec. IV, the QM/MM linking function of Ref. 8 is used in the conv-QM/MM simulations. In both simulations, the temperature quickly equilibrates to half the initial temperature (Fig. 9(a), upper panel) as before. In the bf-QM/MM simulation, the subsequent dynamical evolution is very similar to the reference QM case, with the same Si–O bond at the crack-tip breaking at a very similar strain. The final geometries in Figs. 9(c) and 9(e), and the bond length evolution in Fig. 9(a) show excellent agreement. In the conv-QM/MM case, however, we observe detachment of the QM and MM regions when the strain reaches $\sim 29\%$. This results in exothermic bond breaking leading to a large temperature rise (Fig. 9(a)), and occurs both with the QM/MM linking function of Ref. 8 and with an alternative harmonic link function (see Sec. IV). By constraining the QM-MM linking bonds, this detachment can of course be prevented, but the trajectory evolution does not then follow that of the reference QM calculation. A similar

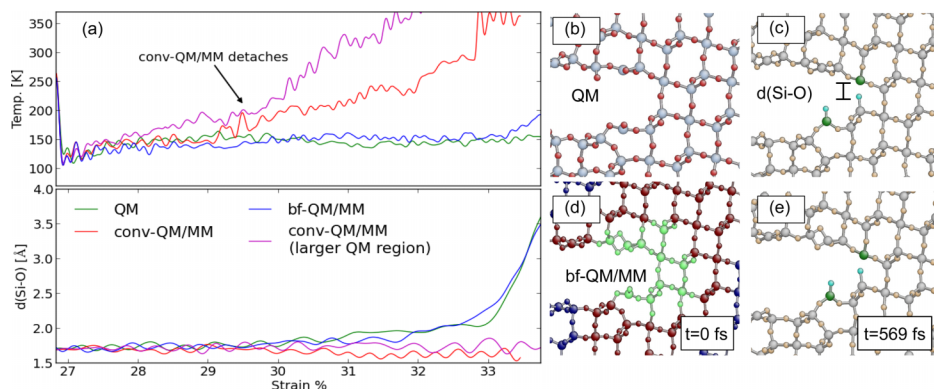


FIG. 9. (a) Evolution of temperature (top) and breaking-bond distance $d(\text{Si-O})$ as a function of the applied strain in the crack propagation simulations. Snapshots of the simulations at $t=0$ and $t=569 \text{ fs}$ (shortly after the bond-breaking event): full QM simulation ((b) and (c)) and bf-QM/MM simulation ((d) and (e)). In panel (b), the color code refers to the atomic species, while in panels (c) and (e), atoms are colored according to their coordination (see Fig. 8). In panel (d), green, red, and blue spheres represent QM, buffer, and MM atoms, respectively.

detachment of the QM and MM regions occurs with a larger QM region, corresponding to the same computational cost as the bf-QM/MM simulation (i.e., a QM region including both the QM core and buffer atoms in Fig. 9(c)). We speculate that the large force errors near the boundary and the fixed parametrization of the QM/MM linking term contribute to this incorrect response.

VII. CONCLUSIONS

We have reported a series of tests which taken together demonstrate that the adaptive buffered force mixing approach can be applied to perform accurate QM/MM calculations in silica. We find that QM forces remain local properties despite the long-range nature of electrostatic interactions but that the length scale is significantly longer than that found for covalent materials. This leads to a requirement for buffer regions with widths of ~ 10 Å rather than ~ 5 Å commonly used for silicon and water. In some cases, electrostatic embedding with the MM point charges as additional contributions to the QM Hamiltonian somewhat improves the convergence of forces evaluated using a finite QM region to the values that would be obtained in a full QM calculation, especially if the embedding charges are chosen to reproduce the correct QM electronic structure (measured here by Mulliken population analysis). However, we show that the contribution of electrostatic embedding (as opposed to simple cluster embedding) to the accuracy of the bf-QM/MM forces is less relevant than the contribution of the buffer region. A more complex electrostatic embedding scheme, such as including higher order multipole moments, might improve this.

The selection of whether it is most efficient to use conventional or adaptive buffered QM/MM depends on the physical problem of interest. For the geometry optimization of the oxygen vacancy, for which the conv-QM/MM scheme was previously tested, we found that the incorrect forces which are invariably present near to the boundary of a conv-QM/MM do not have a significant influence on the geometry obtained at the potential energy minimum. For quasi-static bond-elongation simulations and MD simulations of crack propagation, where the force errors due to the QM/MM boundary are more important, using the buffered approach, which gives accurate forces everywhere, leads to results in much closer agreement with those obtained in reference full QM calculations. Moreover, using the buffered-force approach allows for more flexibility as dedicated potential energy terms that link QM and MM atoms are not required and the region which is treated at the QM level can be redefined during the course of a simulation.

ACKNOWLEDGMENTS

This work was funded by the European Commission (FP7-NMP Grant No. 229205 ADGLASS). J.R.K. and A.D.V. acknowledge funding from the EPSRC HEmS Grant No. EP/L014742/1 and from the Rio Tinto Centre for Advanced Mineral Recovery based at Imperial College, London. J.R.K. additionally acknowledges funding from EPSRC Grant No. EP/L027682/1. L.C.C. acknowledges additional funding from

the DFG Emmy Noether program (Grant No. CI 144/2). The authors acknowledge helpful discussions with Gábor Csányi, Noam Bernstein, Teodoro Laino, and Michael Moseler. This research used computational resources of the Jülich Supercomputing Centre (JSC) (JuRoPa supercomputer). An award of computer time was provided by the Innovative and Novel Computational Impact on Theory and Experiment (INCITE) program. This research used resources of the Argonne Leadership Computing Facility, which is a DOE Office of Science User Facility supported under Contract No. DE-AC02-06CH11357.

- ¹K. Burke, *J. Chem. Phys.* **136**, 150901 (2012).
- ²N. Bernstein, J. R. Kermode, and G. Csányi, *Rep. Prog. Phys.* **72**, 026501 (2009).
- ³H. M. Senn and W. Thiel, *Angew. Chem., Int. Ed.* **48**, 1198 (2009).
- ⁴B. A. Szost, R. H. Vegter, and P. E. J. Rivera-Díaz-Del-Castillo, *Mater. Trans. A* **44**, 4542 (2013).
- ⁵C. Woodward and S. I. Rao, *Phys. Rev. Lett.* **88**, 216402 (2002).
- ⁶J. R. Kermode, T. Albaret, D. Sherman, N. Bernstein, P. Gumbsch, M. C. Payne, G. Csányi, and A. De Vita, *Nature* **455**, 1224 (2008).
- ⁷A. Warshel and M. Levitt, *J. Mol. Biol.* **103**, 227 (1976).
- ⁸F. Zipoli, T. Laino, A. Laio, M. Bernasconi, and M. Parrinello, *J. Chem. Phys.* **124**, 154707 (2006).
- ⁹J. C. Fogarty, H. M. Aktulga, A. Y. Grama, A. C. T. van Duin, and S. A. Pandit, *J. Chem. Phys.* **132**, 174704 (2010).
- ¹⁰J. R. Kermode, S. Cereda, P. Tangney, and A. De Vita, *J. Chem. Phys.* **133**, 094102 (2010).
- ¹¹L. Pastewka, A. Klemenz, P. Gumbsch, and M. Moseler, *Phys. Rev. B* **87**, 205410 (2013).
- ¹²J. Q. Broughton, F. F. Abraham, N. Bernstein, and E. Kaxiras, *Phys. Rev. B* **60**, 2391 (1999).
- ¹³N. Bernstein and D. W. Hess, *Phys. Rev. Lett.* **91**, 025501 (2003).
- ¹⁴G. Csányi, T. Albaret, M. C. Payne, and A. De Vita, *Phys. Rev. Lett.* **93**, 175503 (2004).
- ¹⁵R. E. Buló, B. Ensing, J. Sikkema, and L. Visscher, *J. Chem. Theory Comput.* **5**, 2212 (2009).
- ¹⁶H. C. Watanabe, T. Kubař, and M. Elstner, *J. Chem. Theory Comput.* **10**, 4242 (2014).
- ¹⁷N. Bernstein, C. Várnai, I. Solt, S. A. Winfield, M. C. Payne, I. Simon, M. Fuxreiter, and G. Csányi, *Phys. Chem. Chem. Phys.* **14**, 646 (2012).
- ¹⁸P. Sherwood, A. H. de Vries, M. F. Guest, G. Schreckenbach, C. R. A. Catlow, S. A. French, A. A. Sokol, S. T. Bromley, W. Thiel, A. J. Turner, S. Billeter, F. Terstegen, S. Thiel, J. Kendrick, S. C. Rogers, J. Casci, M. Watson, F. King, E. Karlsen, M. Sjøvoll, A. Fahmi, A. Schäfer, and C. Lennartz, *J. Mol. Struct.: THEOCHEM* **632**, 1 (2003).
- ¹⁹T. Laino, F. Mohamed, A. Laio, and M. Parrinello, *J. Chem. Theory Comput.* **2**, 1370 (2006).
- ²⁰A. Laio, J. VandeVondele, and U. Röthlisberger, *J. Chem. Phys.* **116**, 6941 (2002).
- ²¹M. J. Buehler, A. C. T. van Duin, and W. A. Goddard, *Phys. Rev. Lett.* **96**, 095505 (2006).
- ²²G. Moras, L. Colombi Ciacchi, C. Elsässer, P. Gumbsch, and A. De Vita, *Phys. Rev. Lett.* **105**, 075502 (2010).
- ²³J. R. Kermode, L. Ben-Bashat, F. Atrash, J. Cilliers, D. Sherman, and A. De Vita, *Nat. Commun.* **4**, 2441 (2013).
- ²⁴A. Gleizer, G. Peralta, J. R. Kermode, A. De Vita, and D. Sherman, *Phys. Rev. Lett.* **112**, 115501 (2014).
- ²⁵P. V. Sushko and I. V. Abarenkov, *J. Chem. Theory Comput.* **6**, 1323 (2010).
- ²⁶T. Laino, D. Donadio, and I.-F. W. Kuo, *Phys. Rev. B* **76**, 195210 (2007).
- ²⁷T. A. Michalske and S. W. Freiman, *Nature* **295**, 511 (1982).
- ²⁸C. Várnai, N. Bernstein, L. Mones, and G. Csányi, *J. Phys. Chem. B* **117**, 12202 (2013).
- ²⁹J. VandeVondele, M. Krack, F. Mohamed, M. Parrinello, T. Chassaing, and J. Hutter, *Comput. Phys. Commun.* **167**, 103 (2005).
- ³⁰J. Hutter, M. Iannuzzi, F. Schiffmann, and J. VandeVondele, *Wiley Interdiscip. Rev.: Comput. Mol. Sci.* **4**, 15 (2014).
- ³¹J. P. Perdew, K. Burke, and M. Ernzerhof, *Phys. Rev. Lett.* **77**, 3865 (1996).
- ³²S. Goedecker, M. Teter, and J. Hutter, *Phys. Rev. B* **54**, 1703 (1996).
- ³³J. VandeVondele and J. Hutter, *J. Chem. Phys.* **127**, 114105 (2007).
- ³⁴B. W. H. van Beest, G. J. Kramer, and R. A. van Santen, *Phys. Rev. Lett.* **64**, 1955 (1990).

- ³⁵A. A. Hassanali and S. J. Singer, *J. Phys. Chem. B* **111**, 11181 (2007).
- ³⁶G. Csányi, S. Winfield, J. Kermode, A. De Vita, A. Comisso, N. Bernstein, and M. Payne, *IoP Computational Physics Newsletter*, Spring, 2007.
- ³⁷L. Mones, A. Jones, A. W. Götz, T. Laino, R. C. Walker, B. Leimkuhler, G. Csányi, and N. Bernstein, “The adaptive buffered force QM/MM method in the CP2K and AMBER software packages,” *J. Comput. Chem.* (published online); e-print [arXiv:1409.5218](https://arxiv.org/abs/1409.5218) [physics.chem-ph].
- ³⁸E. Bitzek, P. Koskinen, F. Gähler, M. Moseler, and P. Gumbsch, *Phys. Rev. Lett.* **97**, 170201 (2006).
- ³⁹H. Lin and D. G. Truhlar, *Theor. Chem. Acc.* **117**, 185 (2007).
- ⁴⁰E. R. Cruz-Chu, A. Aksimentiev, and K. Schulten, *J. Phys. Chem. B* **110**, 21497 (2006).
- ⁴¹M. A. Zwijnenburg, S. T. Bromley, C. van Alsenoy, and T. Maschmeyer, *J. Phys. Chem. A* **106**, 12376 (2002).
- ⁴²P. Tangney and S. Scandolo, *J. Chem. Phys.* **117**, 8898 (2002).
- ⁴³D. J. Cole, M. C. Payne, G. Csányi, S. M. Spearing, and L. Colombi Ciacchi, *J. Chem. Phys.* **127**, 204704 (2007).
- ⁴⁴G. Csányi, T. Albaret, G. Moras, M. C. Payne, and A. De Vita, *J. Phys.: Condens. Matter* **17**, R691 (2005).
- ⁴⁵G. Moras, R. Choudhury, J. R. Kermode, G. Csányi, M. C. Payne, and A. De Vita, *Trends in Computational Nanomechanics: Transcending Length and Time Scales* (Springer, 2010).
- ⁴⁶We note that in the bf-QM/MM case, the QM core region does not need to be terminated with O^{*} pseudoatoms (only the larger region consisting of the core and the buffer regions is O^{*}-terminated). As a result, in this test system, a 44-atom QM core region in bf-QM/MM corresponds to a 50-atoms, O^{*}-terminated QM region in the conv-QM/MM scheme.